Northeast Journal of Complex Systems (NEJCS)

Volume 6
Number 1 *Special Issue: NERCCS 2024 Papers*

Article 5

June 2024

Performance Studies of an Axial Flow Waterjet Pump Using an Unsteady Reynolds-Averaged Navier-Stokes Model

Stephen E. Monroe
Clarkson University, monroese@clarkson.edu

Junfeng Wang
Simerics Inc, jw@simerics.com

Chunlei Liang
Clarkson University, cliang@clarkson.edu

Performance Studies of an Axial Flow Waterjet Pump Using an Unsteady Reynolds-Averaged Navier-Stokes Model

Stephen E. Monroe[1], Junfeng Wang[2] and Chunlei Liang[1*]

[1] Mechanical and Aerospace Engineering, Clarkson University, Potsdam, New York, 13699

[2] Simerics Inc, Bellevue, WA 98004

[*] cliang@clarkson.edu

Abstract

In this study, an Unsteady Reynolds-Averaged Navier-Stokes (URANS) model is demonstrated its suitability for studying the flow and performance of open marine propellers and waterjet pumps. First, the accuracy of the URANS model is validated by studying turbulent flow past counter-rotating propellers (CRPs). Specifically, experimental data from Miller (1976) is employed for comparison against the URANS results. Subsequently, URANS is used to study the flow and performance of an Office of Naval Research (ONR) axial flow waterjet pump (AxWJ-2). Due to the large number of degrees of freedom for both simulations, parallel computations over 80 cores are performed. For the CRP study, torque and thrust coefficients are assessed against a range of advance ratios, ensuring a Reynolds number of less than 600,000. For the waterjet, torque and head coefficients are computed for a range of flow rates at a Reynolds number of 1.25 million. For both studies, two levels of mesh resolution are utilized. The finer meshes of both studies contained roughly four times the total number of cells employed in their respective coarser counterparts. These refinements lead to minor improvements, suggesting good grid resolutions with the coarser grids. Across all advance ratios for the CRP set, the URANS torque and thrust coefficients show good agreement with experimental results, remaining within 10% difference. The torque and head coefficients for the waterjet displayed even better agreement, with the greatest error across all flow conditions remaining under 3%. Moreover, URANS studies revealed that the stator is responsible for 20% of the waterjet's power production.

1 Introduction

The idea of enforcing a rotational motion to fluids to achieve work was first realized by Greek mathematician Archimedes around the year 200 BC when he created the first screw propeller. While current propulsion devices look almost nothing like this early development, we still use this very principle to achieve an unquantifiable number of tasks, one of which being marine propulsion. As such, developing better, more efficient marine propulsion systems have been one of humanity's longest-going engineering challenges. All propulsion systems consist of a rotating device used to control the fluid flow. These devices require an input of power and are considered as active flow control devices and in the past, almost all attention went into optimizing the shape of these active flow control devices. However, more and more recent propulsion devices utilize a kind of flow control that requires no input power, known as passive flow control devices. These devices on average increase performance across all operating conditions but are designed to optimize the performance at a specific operating condition, known as the design condition.

The advancements in CFD have revolutionized the design and analysis of both propeller and waterjet pumps. Each propulsion system comes with its own set of advantages and disadvantages, necessitating careful consideration of various factors such as vessel requirements, operational conditions, performance goals, and environmental concerns. Propellers excel in efficiency at lower speeds and in calm waters, making them ideal for long-range cruising. Their simplicity in design and operation translates to lower maintenance costs and requirements, while their ability to generate high levels of thrust suits them well for larger vessels requiring substantial propulsion power. On the other hand, waterjets offer unparalleled maneuverability, enabling operations in shallow waters and executing high-speed turns with ease. Their reduced hydrodynamic drag at high speeds contributes to improved efficiency and overall speed performance. Moreover, waterjets boast lower noise and vibration levels compared to propellers, making them suitable for missions demanding reduced acoustic signatures. However, both systems face challenges at high speeds due to the phenomenon of cavitation, which can degrade reliability, efficiency, and incur high maintenance costs. While the URANS model suffices for predicting pump performance in engineering design parameterization, more advanced and robust LES models are essential for accurately predicting cavitation, noise generating vortices, and energy losses. Recently, Monroe [3] reported an extensive comparative study of the flow and performance of the waterjet pump using a large eddy simulation technique of Open-FOAM.

In the present study, SimericsMP+, a commercial Unsteady Reynolds-Averaged Navier-Stokes solver is used. The standard $k - \epsilon$ and the Renormalization Group (RNG) $k - \epsilon$ turbulence closure models are used. Validation of the URANS model

with mismatching-grid interfaces (MGI) involves comparing the URANS results of a marine propeller set against experimental data using the standard $k-\epsilon$ model. Subsequently, the standard $k-\epsilon$ URANS model and the RNG $k-\epsilon$ model are used to analyze the AxWJ-2 pump at varying advance coefficients. Simerics Inc stands out as a prominent developer, marketer, and supporter of Computer- Aided Engineering (CAE) software crafted for the virtual simulation and testing of pumps, valves, compressors, motors, and systems [25]. The company's CAE toolset comprises two sophisticated offerings: Simerics-MP and Simerics-MP+. While Simerics-MP is tailored for Multi-Purpose applications, Simerics-MP+ introduces enhanced features such as streamlined setup procedures, automated mesh/re-mesh functionalities designed for key components in motion, and customized data reduction processes. This comprehensive suite strategically positions Simerics as a pivotal player in the domain of virtual simulation for fluid dynamics applications.

This paper is organized as follows. Section 2 describes validation using DTMB CRP6. Section 3 contains the performance study of AxWJ-2 and the effect of varying operating conditions. A comparison of the standard $k-\epsilon$ and RNG $k-\epsilon$ models is also conducted. Section 4 compares the performance of the waterjet pump with and without the stator component. The last section summarizes the results and conclusions.

2 Validation study using DTMB CRP6

Before simulating the AxWJ-2, simulations of the DTMB CRP6 are conducted to validate the URANS model and confirm its capability to analyze the complex flow characteristics of the AxWJ-2. With nearly four decades of history, the DTMB CRP6 has undergone thorough experimental testing by Miller [2], establishing its benchmark status and making it an ideal choice for validating the URANS solver.

The CRP configuration shown in Figure 1 features two four-bladed propellers axially spaced 1.7 inches (0.28R) apart, representing one of the smallest axial spacings in the DTMB CRP series. This choice suggests a highly strained flow, providing valuable insights into the MGI technique's ability to handle high shearing flows. Key geometric parameters of the CRP set are outlined in Monroe's M.S. thesis [3].

To validate the combination of the URANS model with thhe MGI technique, initial simulations were conducted by comparing the thrust coefficient K_T and the torque coefficient K_Q measurements at the design condition, refining the technique until the solution error was minimized. Once the design condition achieved satisfactory results, subsequent validation involved maintaining constant rotational speeds while altering the advance ratio to align with those studied by Miller [2].

The MGI technique demonstrates its innovative approach by capitalizing on the automated binary-tree mesh generation process inherent in Simerics' mesh gener-

Figure 1: Perspective view of CRP6

ator. Through clever use of the binary tree data structure, MGI effectively reduces memory access requirements, leading to a significant acceleration of the solution process. Additionally, MGI introduces a newly developed non-conformal grid interface algorithm, efficiently conserving mass and other crucial conservation quantities across grid interfaces. This advanced solver further boosts efficiency with a blended Conjugate Gradient Squared-Algebraic Multi-Grid linear solver, ensuring both accelerated and robust convergence. With this set of features, the MGI algorithm emerges as a potent and efficient tool for fluid dynamics simulations [4].

2.1 Computational domain and mesh generation

As shown in Figure 2, the simulation domain is configured as a cylinder with a streamwise length of 25D and a radius of 8D. While experimental data was performed in a 24 inch diameter testing facility, the domain size was chosen to leverage the success demonstrated by Safford et al [5]. Conversely, domain blockage

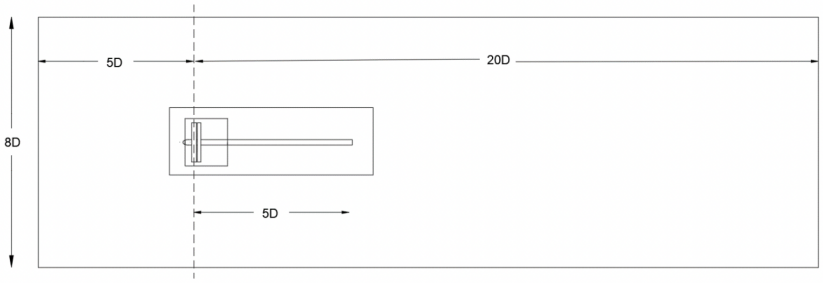

Figure 2: The computational domain for CRP6 and refinement zones for URANS simulations

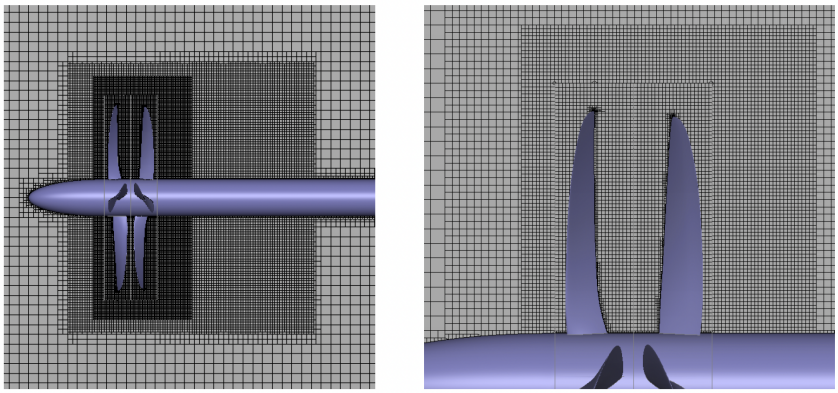

Figure 3: The computational mesh for CRP6 (left) refinement zones, and (right) close-up view of rotating domains.

corrections were not applied to the forcing predictions. The forward propeller, positioned 5D into the domain, extends its shaft 5D downstream. Surrounding the propellers are two cylindrical rotating meshes generated as seen in Figure 2, using Simerics' automated binary-tree mesh generator. While this generator demonstrates extremely high efficiency, it adheres to Octree mesh generation principles, restricting cell size to factors of two and thereby constraining variability and flexibility in cell sizing. Additionally, limited to hexahedrons, this approach fails to fully capture the precise edges of the propellers, resulting in misrepresentations known as 'sub features'. However, the Simerics solver effectively manages these sub features, ensuring a high-fidelity simulation. On the propellers' surface, cells have an approximate size of 0.0016D (0.5 mm), expanding to 0.0066D in the remaining rotating domain, seen in Figure 3. This element size aims to maintain a y+ value of 60, aligning closely with the recommendation by Wang and Xiong [6].

The rotating meshes, with a diameter of 1.1D and a length of 0.15D, comple-

ment the stationary mesh, where elements are 0.01D (32mm) in size. Utilizing Simerics' nested refinement zones, three cylindrical zones enhance flow field resolution around the rotating mesh. The first zone, 0.8D upstream of the propeller, spans 6.5D with a diameter of 2D and a cell size of 0.0052D. The second zone, starting 0.25D upstream, is 1.3D long with a diameter of 1.44D with a cell size of 0.0013D. The last zone, with the same cell size as the rotating domains, is positioned 0.125D upstream and 0.4D downstream of the propeller, with a diameter of 1.4D, ensuring 1:1 face matching between domains.

The mesh configuration utilizes a total of 6.64 million hexahedral elements. The stationary mesh comprises 3.61 million elements, while the forward and aft rotating meshes contain 1.48 and 1.54 million elements respectively. At the design advance ratio, an additional simulation is conducted with the cell size in the rotating domains and the first two refinement zones halved, resulting in a total cell count of 27.35 million—a substantial 300% increase in cells in that specific region.

2.2 Boundary conditions and simulation setup

For the turbulence closure equations, an upwind scheme is implemented. The momentum equations utilize a second-order upwind scheme. Time marching employs the Euler backward differencing scheme, with a time step corresponding to one degree of rotation. Inlet conditions are defined by free stream velocity, while reference pressure is set at the outlet. Slip wall boundary conditions are applied to the cylindrical walls. The shaft is modeled as a no-slip wall, and a rotating no-slip wall is utilized on the propellers and hubs. A standard wall function in the Simerics suite was incorporated in this study to handle near-wall physics efficiently, avoiding the need for a considerable increase in computational resources for full resolution.

To align with the experimental conditions of Miller [2], the propeller rotational speed remained constant at 12 RPS, and inlet speeds were adjusted, resulting in simulations conducted at Reynolds numbers spanning from 510,000 to 580,000 based on the standard definition at r/R = 0.7. The design operating conditions for the propeller are at a Reynolds number 1.38 million with a freestream velocity of 4.03 m/s and a kinematic viscosity of 8.917×10^{-7}. The design advance ratio is 1.1.

As startup transience was of no interest, the domain was initialized with the free stream velocity to expedite the calculation. Additionally, the MRF approach was employed to obtain a steady-state solution, serving as the initial conditions for the subsequent transient simulation. In all simulations of CRP6, the selection of the time-step size further followed the recommendation of Wang and Xiong [31], who explored the role of time-step size and turbulence models in achieving reasonable URANS results for CRPs. A time step of 2.31×10^{-4} seconds was utilized, corresponding to one time-step per degree of rotation. Simulations were executed using

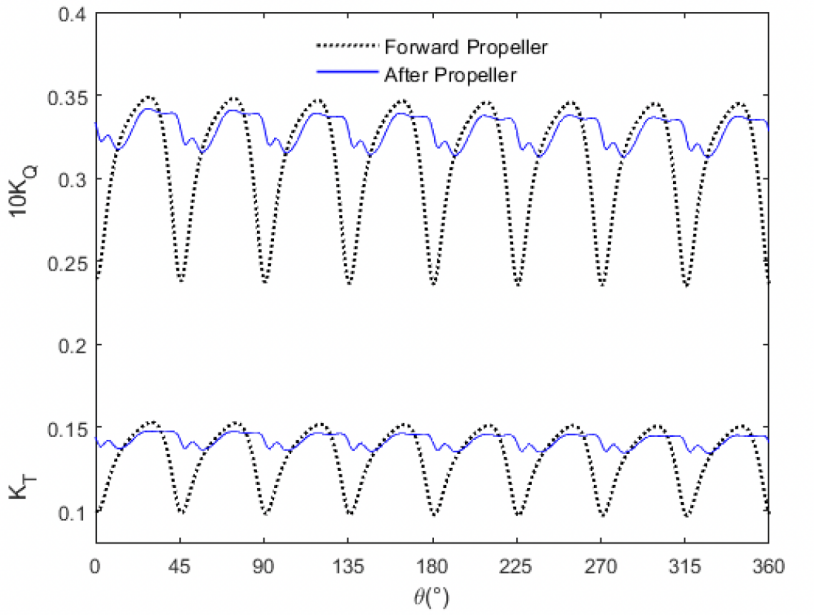

Figure 4: Thrust and torque coefficients for CRP6 as a function of rotation.

as few as 80 parallel processors and as many as 120.

2.3 Validation results

The simulation of CRP6 ceases once the thrust and torque coefficients enter an oscillatory phase, characterized by fluctuations within a certain percentage range around their mean values. This behavior is evident in the results obtained at the design advance ratio, as depicted in Figure 4, which illustrates these oscillations throughout one complete rotation. Notably, when both propellers are rotated by 45 degrees, the thrust and torque of each propeller exhibit repetitive patterns, resulting in 8 peaks per revolution. The amplitude of fluctuations for the forward propeller is approximately 40% of its mean value, nearly four times larger than the 12% fluctuation amplitude observed for the aft propeller.

Based on these findings, the time-averaged values derived from three consecutive rotations are computed for K_T and K_Q. On the forward propeller, the thrust and torque coefficients are determined to be 0.1302 and 0.0305, respectively, while on the aft propeller, they are 0.1398 and 0.0325, respectively. These values fall within a 10% range of the experimental data gathered by Miller [2]. Across all advance ratios, it is inferred that the forward propeller contributes approximately 46% of the total thrust, leaving the remaining 54% to be generated by the aft propeller as shown in Figure 5.

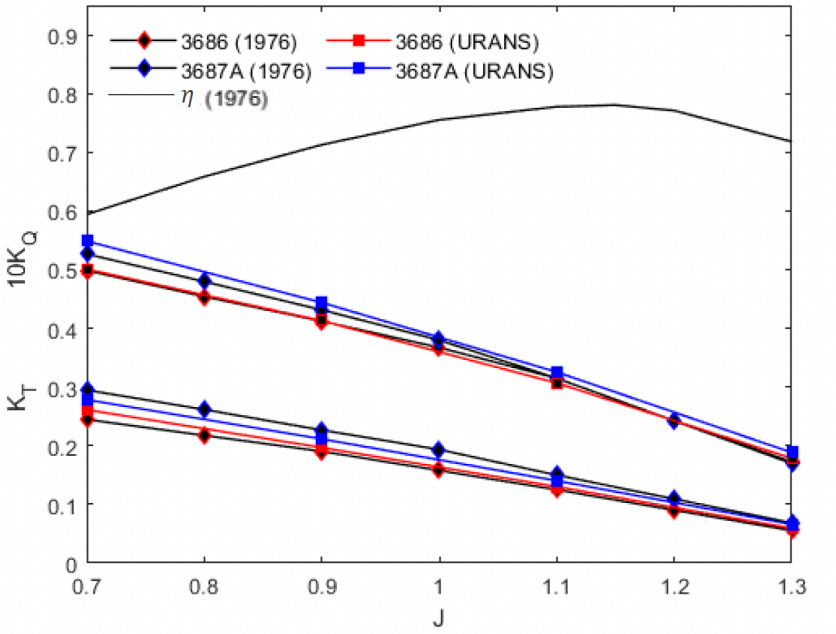

Figure 5: Thrust and torque coefficients for CRP6 as functions of the advance ratio.

The observation of a larger error for the aft propeller is supported by the greater instantaneous surface pressure distribution difference on the aft blades at the design condition, as depicted in Figure 6. This discrepancy is likely a result of the wake induced on the aft propeller by the forward one, leading to increased turbulence and providing explanation for the higher error margins on the aft propeller. Additionally, when operating in overdriven conditions CRP6 loses the torque balance typically desired from contra-rotating propeller systems. This imbalance in torque can be attributed to the higher rotational speeds, which heighten the induced wake and turbulence onto the aft propeller, explaining the increased error margins observed under such conditions.

Despite the challenge in accurately predicting the performance of the aft propeller, all recorded values remain within 10% of the experimental data documented by Miller. Simulations conducted under the design conditions with a finer mesh yielded slightly improved predictions for aft coefficient values and nearly identical predictions for the forward propeller. As a result, confidence is instilled in Simerics' capacity to analyze intricate rotational flows, paving the way for simulations of the waterjet pump to proceed.

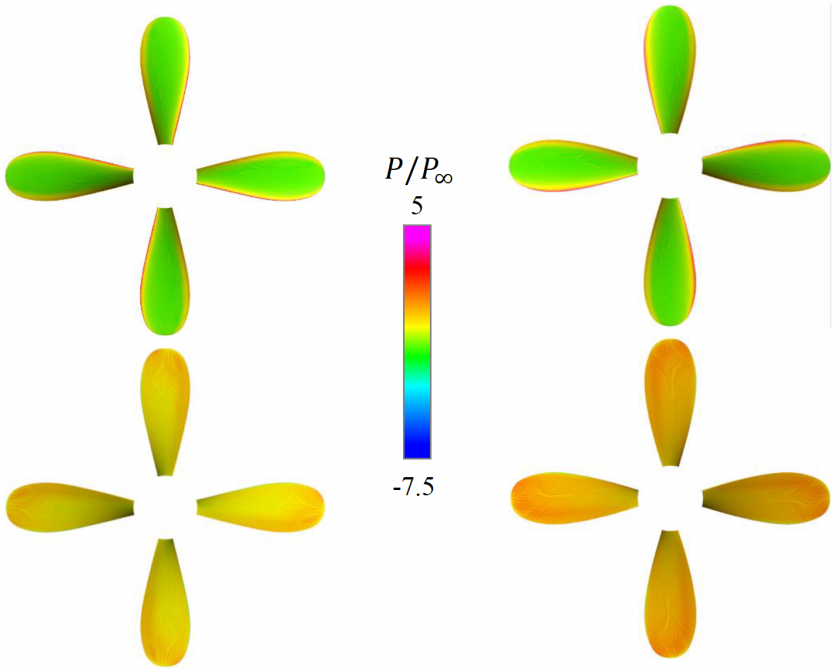

Figure 6: Suction side (top) and pressure side (bottom) instantaneous normalized pressure distributions on forward (left) and aft (right) CRP6 propeller blades.

3 Application to ONR Waterjet AxWJ-2

The AxWJ-2 pump designed by Michael et al [1], features a rotor (5521) with six blades and a stator (5522) with eight blades, as illustrated in Figure 7. The stator is directly mounted on the pump's casing wall.

As detailed in Figure 8, both the rotor and stator utilize a NACA 16 thickness distribution in the chordwise direction, with an Expanded Area Ratio (EAR) of 1.947 and 1.287, respectively. Designed at various model scales for performance testing at different water tunnel facilities, this study employs the 12" (304.8 mm) diameter model, characterized by a 0.5mm gap between rotor blades and casing walls, while the stator is directly mounted to the casing walls. Unlike larger scale models, this version features an increased spacing between the rotor and stator to facilitate experimental data collection, which was deemed insignificant and thus excluded to conserve computational resources. Additionally, the exit nozzle is extended to ensure a uniform pressure field across the exit plane for measurement purposes. As the stator represents the final step in the iterative design process laid out by Michael et al [1], one goal of this study is to understand the stator's role in aiding AxWJ-2's performance.

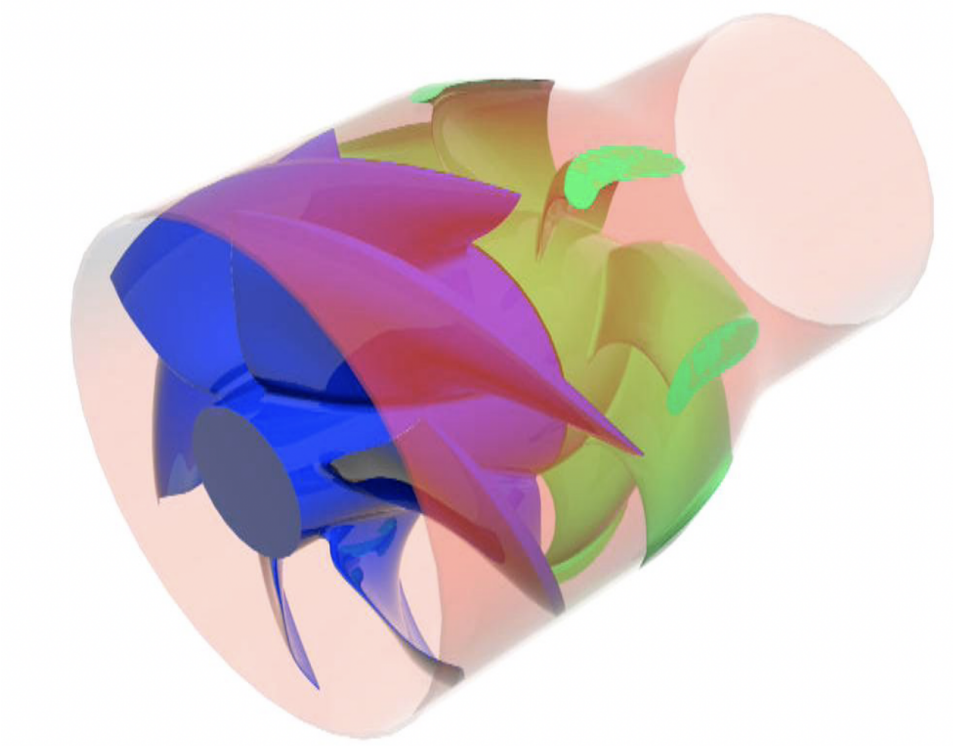

Figure 7: Three-dimensional configuration of the ONR Waterjet AxWJ-2 pump

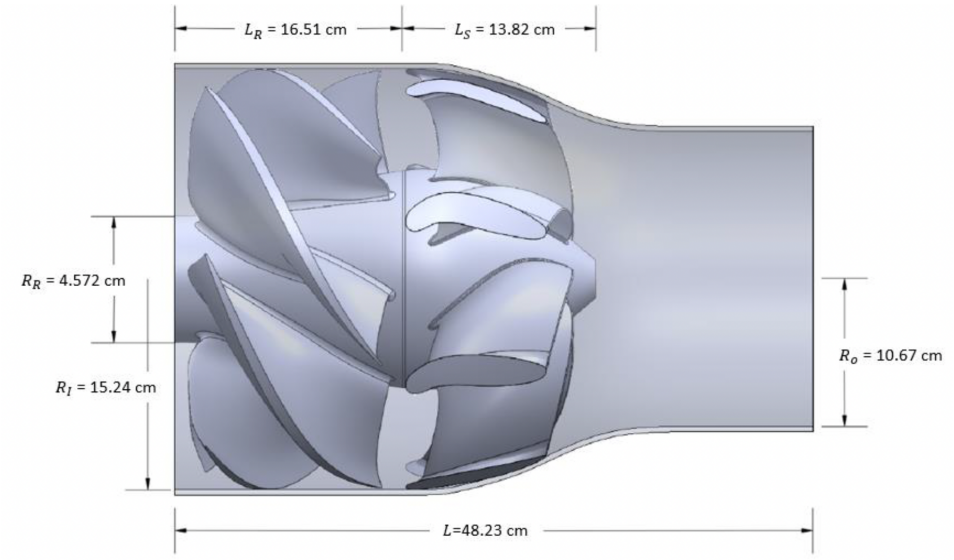

Figure 8: Geometry of ONR Waterjet AxWJ-2

Two important parameters are employed to characterize the operational conditions of the pump. The Reynolds number (4.19 million) utilized for analyzing the waterjet pump differs slightly from that used for the propeller, as it is based on the rotor's tip speed and chord length. The second crucial nondimensional parameter is the flow coefficient, as defined in Eq. 1. Similar to the advance ratio, the flow coefficient Q^* establishes a relationship between the advancing (inlet) speed or volumetric flow rate $\dot{\mathcal{V}}$ and the rotational speed of the rotor.

$$Q^* = \frac{\dot{\mathcal{V}}}{nD^3} \tag{1}$$

In pump flows, the head rise is nondimensionalized into the head coefficient as defined in Eq. 2 where ΔP is the change in total pressure (static and dynamic) between the inlet and outlet of the waterjet pump and D is the inlet diameter.

$$H^* = \frac{\Delta P}{\rho(nD)^2} \tag{2}$$

3.1 Computational domain and mesh for the pump simulations

The computational domain for these simulations is defined by the casing geometry and comprises two separate yet interconnected regions. On the coarse mesh both regions employ a 2 mm element size, while the surfaces of the rotor and stator are composed of 1 mm cells, maintaining an average $y+$ value of 250. Thus, the same standard wall function introduced in Chapter 3.3.2 was reused. Leveraging Simerics' efficient binary tree and sub-feature mesh generation algorithm, these cell sizes result in a conservative total of 3.82 million elements. The stationary mesh consists of 1.98 million elements, with the remaining 1.84 million elements allocated to the rotating mesh surrounding the rotor, reflecting both the difference in blade count between the components and casing dimension. With minimal specification, the Simerics mesher adeptly accommodated the 0.5mm tip gap between rotor blades and casing wall, accommodating a single element in this region. For ease of visualization, Figure 9 displays a cross sectional view of the coarse mesh. Additionally, at the design flow coefficient, an extra simulation is conducted in which all cells except for the rotor tip gap are halved, resulting in a total cell count of 24,589,043, representing approximately a 6.5X increase in cells.

3.2 Boundary conditions and simulation setup

A Dirichlet boundary condition was utilized to prescribe a volumetric flow rate at the inlet, while the outlet was set to a reference pressure. No-slip wall conditions were applied to the casing walls, stator blades, and hub, while a rotating no-slip

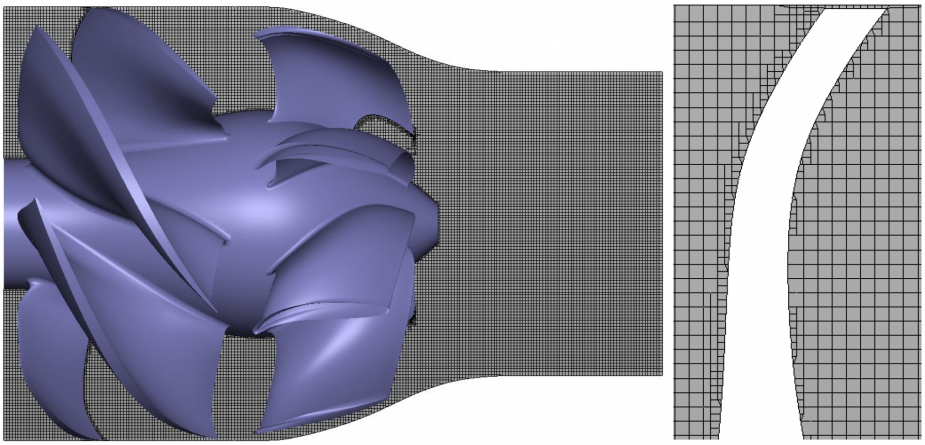

Figure 9: Coarse mesh for ONR Waterjet AxWJ-2

wall was employed on the rotor. To adhere to typical experimental performance testing procedures, the rotor's rotational speed was maintained at a constant 2000 RPM, with adjustments made to the inlet mass flow rates, facilitating simulations conducted across Reynolds numbers ranging from 2.93×10^6 to 4.68×10^6. As startup transience was of no interest, the methodology outlined in previous validation section for CRP6 was replicated. Primarily, the domain was initialized with the free stream velocity to hasten the calculation, and the MRF approach was utilized to achieve a steady-state solution, serving as the initial conditions for the subsequent transient simulation. For all transient simulations of AxWJ-2, insights from the CRP6 study were leveraged, and a time step of 8.33×10^{-5} seconds was adopted, equating to one time-step per degree of rotation. All numerical schemes, under-relaxation factors, convergence criteria, and linear matrix solvers used in AxWJ-2 simulations are consistent with those utilized in CRP6 validation efforts. It was observed that the SIMPLE algorithm produced stable results within 350 iterations for the steady-state MRF solution, while the PISO algorithm in the transient simulations took an average of 7 iterations to converge for each time-step.

3.3 Results for the waterjet pump

An instantaneous snapshot of the streamlines and averaged pressure distribution from the URANS calculation is shown in Figure 10. As the rotor undergoes rotation, the average downstream total pressure just beyond the rotor increases significantly, by a factor of 20, resulting in a heightened intake of fluid into the rotor. Maintaining a small gap between the rotor blade and casing wall is crucial to maximize the rotor's efficiency in performing work. This narrow clearance generates

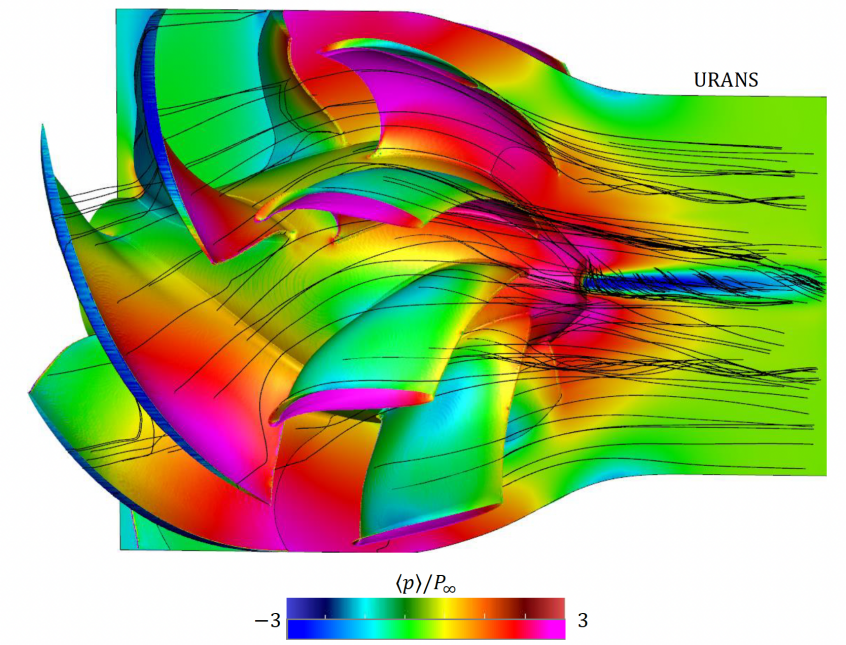

Figure 10: Streamlines and normalized pressure distribution around the rotor and the stator in the ONR pump

pressures between the blade tips and casing wall that are 180 times greater than freestream, effectively doubling the flow speed from 11 to 21 m/s and generating over 1100 N-m of torque on the redirected stator. As the flow is redirected, the casing undergoes a reduction in size by a factor of 1.4, further accelerating the flow to an exit velocity of 22 m/s.

Given the likelihood of varying operating conditions for the waterjet, it is essential to investigate its performance across a range of flow coefficients and discern the factors influencing deviations in performance. Figure 11 and Figure 12 illustrate the significant influence of the stator on deviations in performance from the design flow coefficient, elucidating distinct performance trends. Specifically, at flow coefficients below design, i.e. in overdriven conditions, the rotor over rotates the flow for the incoming speed, which leads to the streamlines appearing steeper as they come off the blades. When interacting with the stator at this sub-ideal trajectory, the flow separates and subsequently recirculates on the trailing edge, which can be seen in both the curling streamlines in Figure 11 and in Figures 12(a) and 12(b), leading to a reduction in torque and efficiency.

Conversely, at flow coefficients surpassing design specifications, i.e. in under driven conditions, the blades rotate at an insufficient rotational rate, which causes these streamlines to come in at a shallower trajectory. This again leads to insuffi-

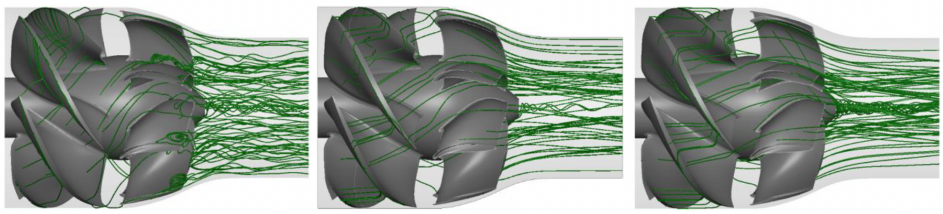

Figure 11: Streamliens around rotor and stator blades at three different flow coefficients. Left panel: $Q^* = 0.595$, middle panel: $Q^* = 0.85$, right panel $Q^8 = 1.02$.

cient redirection by the stator, resulting excessive swirling as seen in Figure 11 and in the thicker slowed velocity region in Figures 11 and 12(f). In both instances, the flow interacts with the stator in a suboptimal manor and leads to a drop in both pressure change and efficiency, underscoring the precision and intricacy of the design. These observations are further encapsulated in Figure 13, which underscores the notable achievement of AxWJ-2, demonstrating peak applied torque attainment remarkably close to the design flow coefficient of 0.85, thereby affirming its commendable design.

As a general trend, at flow coefficients below design, the fluid swirls excessively, which leads to a drop in applied torque and decrease in efficiency. At flow coefficients above design, the blades fail to spin fast enough to effectively do work to the fluid which corresponds to a drop in both applied torque and head and in turn, efficiency. These trends are summarized in Figure 13, where it is clear that a maximum applied torque is achieved very close to the design flow coefficient, 0.85, confirming that AxWJ-2 is well designed.

For comparative studies, Monroe [3] also conducted large eddy simulations (LES) of this pump using a dynamic subgrid-scale model in Open-FOAM. Interestingly, both URANS and LES simulations indicate that the stator counteracts a greater amount of torque than what is produced by the rotor. This observation is prominently illustrated in Figure 14, depicting the torque values of the rotor and stator obtained from URANS and ELES simulations on the coarse grids, covering a time range for tU_∞/D from 1.2 to 4.8 for 3 revolutions. In this figure, the stator torque oscillation amplitude is much higher in magnitude, an observation likely explained by the trailing edge flow separation. URANS simulations suggest that this counteraction amounts to nearly 9.6% more torque than what the rotor generates, while ELES simulations indicate a value of 3.3%. Despite its small magnitude, the occurrence of this phenomenon across both simulation types and grid resolutions suggests its physical nature, possibly attributed to the casing undergoing a reduction in size by a factor of 1.4, leading to further flow acceleration to an exit velocity of 22 m/s.

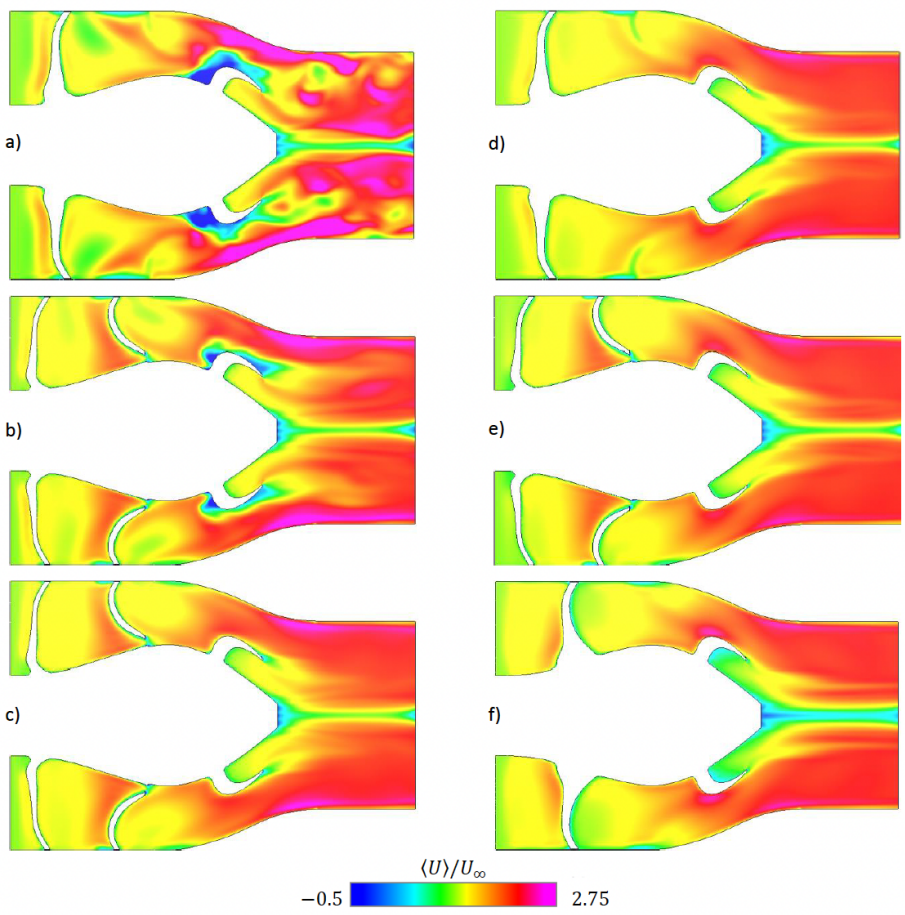

Figure 12: Normalized instantaneous velocity contours of AxWJ-2 with Q^* = a) 0.595 b) 0.680 c) 0.765 d) 0.85 e) 0.935 f) 1.02 on URANS coarse grid

Investigating the contributions of the stator and extended nozzle to waterjet performance is of particular interest for our URANS studies. Therefore, simulations were conducted with these elements excluded. Meshing and simulation settings remained consistent with those used in the full geometry study, with simulations conducted at the design flow coefficient. At this coefficient, removing the extension of the exit nozzle had minimal impact on waterjet performance, resulting in only a 2% increase in normalized head. This marginal alteration was anticipated, as the nozzle extension was primarily implemented to ensure a uniform pressure distribution for the ease of experimental data collection—a task it effectively achieved. However, removing the stator resulted in a significant decline in waterjet performance. At the design flow coefficient, it was observed that the waterjet produced a 20% lower pressure difference when the stator was omitted. This underscores the

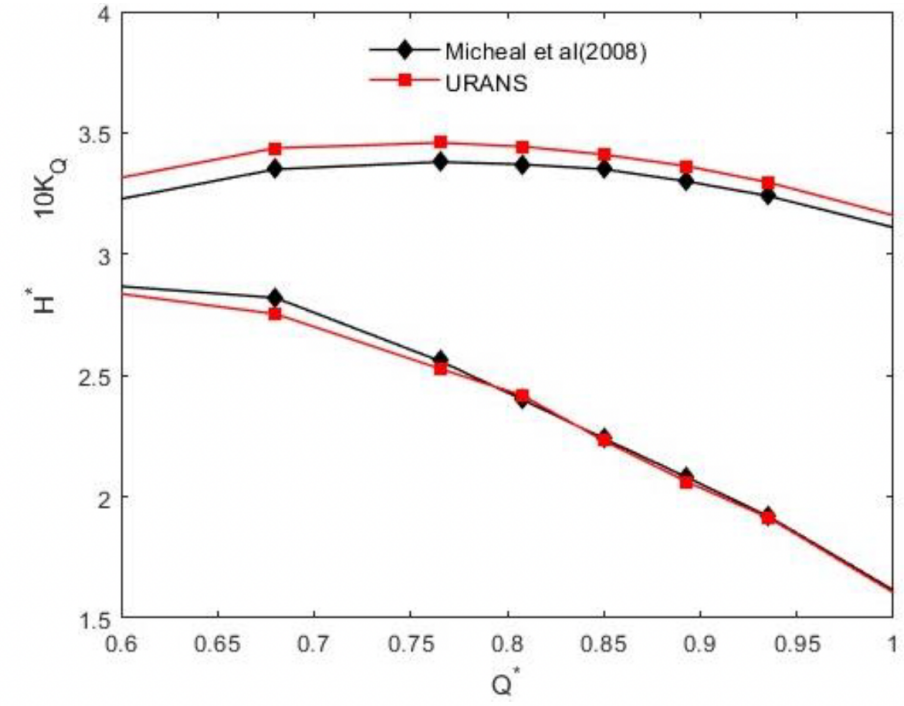

Figure 13: Head coefficient and torque coefficient of the waterjet pump running at different flow coefficients.

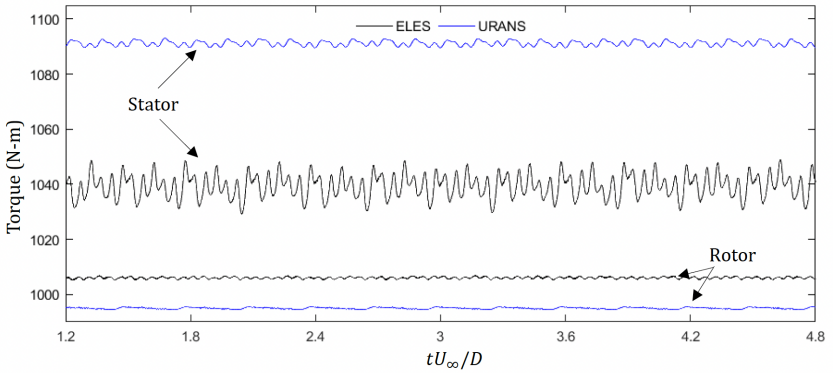

Figure 14: Torque production comparison between rotor and stator blades

substantial role played by the stator in waterjet performance, as its absence leads to a loss of axial redirection for the swirling fluid, thereby wasting much of the imparted energy. This redirection effect is illustrated in Figure 15.

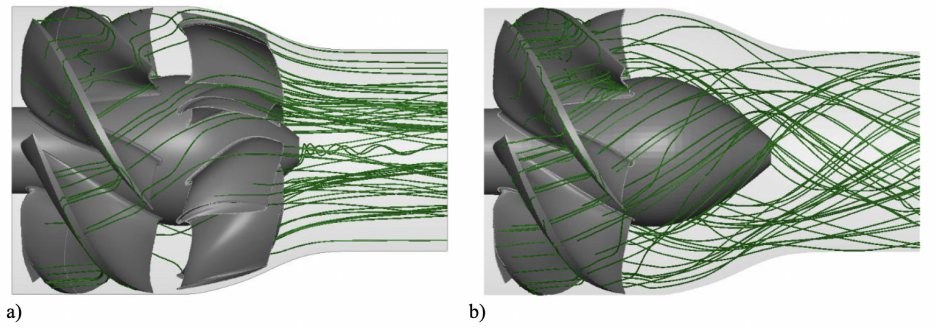

Figure 15: Streamlines in the waterjet pump with stator versus without stator

4 Conclusions

The URANS models in SimericsMP+ offer a swift and reasonably accurate method for analyzing turbulent flows involving rotating geometries. Utilizing the Simerics software, complex geometries were effectively resolved, yielding high-fidelity results within a short timeframe and with a moderate number of computer processors. URANS demonstrated the capability to predict torque and thrust coefficients for the DTMB CRP6 marine propeller set within a 10% difference from experimental data, while reproducing numerical results for AxWJ-2 within a 3% margin in comparison with designed goals. This combination of speed and accuracy renders URANS a valuable tool for studying waterjet fluid dynamics. One significant finding from this study highlights the crucial role of the stator. The absence of stator redirection results in nearly a 20% reduction in power output, indicating its substantial impact. This redirection effect mirrors the concept of incorporating a counter-rotating propeller in a conventional propeller system, albeit with a more pronounced effect. Furthermore, it can be inferred that AxWJ-2 is exceptionally well-designed, as it achieves maximum torque and efficiency under design conditions according to URANS results.

Acknowledgments

The authors including Monroe and Liang would like to thank Dr. Scott Black and Dr. Thad Michael of Naval Surface Warfare Center (NSWC), Carderock Division for providing us with the designed geometry of the waterjet pump. The first author was supported by a graduate teaching assistantship throughout his M.S. program at Clarkson University.

References

[1] T.J. Michael, S.D. Schroeder, and A. J. Becnel. Design of the ONR AxWJ-2 axial flow water jet pump. Technical Report NSWCCD-50-TR-2008/066, Naval Surface Warfare Center Carderock Division, 2008.

[2] M. L. Miller. Experimental determination of unsteady forces on contrarotating propellers in uniform flow. Technical Report Report Number 659-01, David Taylor Research and Development Center, 1976.

[3] S.E. Monroe. URANS and LES studies of turbulent flows in an ONR waterjet pump using unstructured grids with sliding mesh interfaces. Master's thesis, Clarkson University, Potsdam NY, 2024.

[4] A. Pandey, J. Wang, R. V. Godavarthi, and D. Maiti. Performance and validation of a segregated pressure-based solver for computations of low and high-speed compressible flows. *AIAA paper*, pages 2023–2274, 2023.

[5] D. A. Safford, J. Wang, C. Liang, and K. Visser. Unsteady Reynolds-Averaged Navier–Stokes Simulations of a Ducted Wind Turbine. *Journal of Fluids Engineering*, 146(3):031202, 2024.

[6] Z. Wang and Y. Xiong. Effect of time step size and turbulence model on the open water hydrodynamic performance prediction of contra-rotating propellers. *Chinese Ocean Engineering*, 27:193–204, 2012.